




Phase transition and optical properties of samarium-doped BiFeO₃ nanoparticles

Mekonnen Tefera Kebede¹, Venus Dillu^{2,*} , Sheela Devi³, and Sunil Chauhan²

¹Department of Nano-Science and Technology, School of Basic Sciences and Research, Sharda University, Greater Noida, UP 201310, India

²Department of Physics, School of Basic Sciences and Research, Sharda University, Greater Noida, UP 201310, India

³Department of Applied Sciences, Maharaja Surajmal Institute of Technology, C-4, Janakpuri, New Delhi 110058, India

Received: 28 May 2020

Accepted: 18 September 2020

Published online:
27 September 2020

© Springer Science+Business
Media, LLC, part of Springer
Nature 2020

ABSTRACT

Multiferroics are the materials having ferroelectric and magnetic properties simultaneously and can be tuned by controlling electric and magnetic field for the desired applications. Pure and samarium-doped bismuth ferrite nanoparticles Bi_{1-x}Sm_xFeO₃ (BSFO $x = 0, 0.05, 0.10, 0.15, 0.20$) with varied doping concentrations have been synthesized using sol-gel technique. The effect of doping on structural, morphological, elemental composition and optical properties were analyzed using various characterization techniques. X-ray diffraction (XRD) analysis of Bi_{1-x}Sm_xFeO₃ samples show the compressive lattice distortion and structural phase transformation from rhombohedral to orthorhombic phase. The Rietveld refinement shows that the crystalline structure of pristine BiFeO₃ (BFO) is typical rhombohedral structure with R3c space group. Scanning electron micrograph (SEM) reveals that with increasing Sm concentration the grain size decreases up to ~ 30 nm. XRD and SEM analysis confirmed the synthesized samples having pure phase formation and nanocrystalline nature. Ultraviolet-Visible (UV-Vis) spectra of the samples show that the enhanced visible light absorption would be a promising material for photocatalytic application. The findings of X-ray photoelectron spectroscopy (XPS) verify the effective Sm doping in BFO samples.

1 Introduction

Multiferroics are a crucial class of multifunctional materials in the same phase which have electrical and magnetic properties. These materials are extensively studied in the growing discipline of attenuating

electromagnetic radiation, information storage media, resistive switches, gas sensors and multi-state memory devices, etc. [1–3]. Bismuth ferrite is one of the most promising material and attract extraordinary attention due to the combination of anti-ferromagnetic Neel temperature ($T_N \sim 643$ K) and high

Address correspondence to E-mail: venus.dillu@sharda.ac.in

ferroelectric Curie temperature ($T_C \sim 1143$ K) [1, 4]. It is a G-type antiferromagnet with a symmetry permitted slight canting of the Fe^{3+} moments and ferroelectric properties in BFO are induced by a rhombohedral distorted perovskite structure with space group R3c [5]. Even though R3c symmetry allow the presence of weak ferromagnetic moment and net magnetization for the cause of the Dzyaloshinskii-Moriya (DM) interaction [6, 7]. But this material have limitation of the high leakage current density which prohibits the functional application in the manufacturing of the ferroelectric devices [8, 9]. Therefore, to enhance ferromagnetic property, significant efforts should be carried out to suppress the spiral spin structure or to increase the canting level of the antiparallel spins [10]. In the meantime, it is crucial to investigate how to reduce the leakage current density. The presence of leakage current density of BFO is recognized to be attributable to the chemical valence fluctuation of Fe ions ($\text{Fe}^{3+}/\text{Fe}^{2+}$), oxygen vacancies and the loss of bismuth [11]. It is broadly agreed that innate polarization and magnetization are interconnected with the single pair of Bi^{3+} ion at the A site and the partially filled 3d orbitals of Fe^{3+} ion at the B site, respectively [12]. Basically natural BFO is an insulator with a wide bandgap of 2.5 eV [13]. The photo response of BFO nanoparticles can be enlarged in the ultraviolet and visible region attribute to the fact that the microstructure, chemical structure and defects can be enhanced by doping of rare-earth metal ions [14]. Consequently, there is an increased possibility of utilizing the ultraviolet and visible light for photocatalysis. Physical characteristics of BFO can be monitored by doping which induce the lattice distortion, monitor the vaporization of Bi ions and provide the non-centrosymmetry. In addition, doping at the A site with various ionic radii can make the locked magnetization released by suppressing the spiral spin modulation of G-type antiferromagnetism [6]. As a result, advances in doped nano-sized BFO materials, which play an important role in microelectronics devices, can be made to improve magnetoelectric coupling [15–17].

In this work, nanoparticle BFO and $\text{Bi}_{1-x}\text{Sm}_x\text{FeO}_3$ ($x = 0.00, 0.05, 0.10, 0.15, 0.20$) samples were prepared by a sol-gel method. Sm-doped BiFeO_3 nanoparticle samples were characterized by various techniques including X-ray diffraction (XRD), Scanning electron microscopy (SEM), X-ray photoelectron spectroscopy

(XPS) and UV-Vis spectroscopy. However, the effect of Sm^{3+} doped on structural, chemical element and optical properties of BFO are less identified but Sm doping was implemented to improve optical and multiferroic properties in BFO nanoparticles. Because of the small ion size of Sm^{3+} , the crystal structure was distorted and the non-centrosymmetry of the structure was increased. Here, the effect of Sm-doped BFO nanoparticles on the crystal structure, chemical element and optical property was studied comprehensively, and the findings were discussed in detail.

2 Experimental details

2.1 Materials

Poly vinyl alcohol ($\text{C}_2\text{H}_4\text{O}$), nitric acid (HNO_3), Bismuth (III) nitrate pentahydrate $\text{Bi}(\text{NO}_3)_3 \cdot 5\text{H}_2\text{O}$, Iron (III) nitrate nonahydrate $\text{Fe}(\text{NO}_3)_3 \cdot 9\text{H}_2\text{O}$, Samarium (III) nitrate hexahydrate $\text{Sm}(\text{NO}_3)_3 \cdot 6\text{H}_2\text{O}$ and Tartaric acid $\text{C}_6\text{H}_6\text{O}_7$ were used as a precursor materials for the synthesise of pure and doped bismuth ferrite nanoparticles. These all materials were purchased from Sigma Aldrich and used without any further purification.

2.2 Materials synthesis

$\text{Bi}_{1-x}\text{Sm}_x\text{FeO}_3$ ($x = 0.00, 0.05, 0.10, 0.15, 0.20$) namely, BiFeO_3 (BFO), $\text{Bi}_{0.95}\text{Sm}_{0.05}\text{FeO}_3$ (BSFO-5), $\text{Bi}_{0.90}\text{Sm}_{0.10}\text{FeO}_3$ (BSFO-10), $\text{Bi}_{0.85}\text{Sm}_{0.15}\text{FeO}_3$ (BSFO-15), $\text{Bi}_{0.80}\text{Sm}_{0.20}\text{FeO}_3$ (BSFO-20) were successfully synthesized using the experimentally optimized sol-gel technique with tartaric acid. In this process, precise amount of bismuth nitrate $\text{Bi}(\text{NO}_3)_3 \cdot 5\text{H}_2\text{O}$ ferric nitrate $\text{Fe}(\text{NO}_3)_3 \cdot 9\text{H}_2\text{O}$ and samarium nitrate $\text{Sm}(\text{NO}_3)_3 \cdot 6\text{H}_2\text{O}$ were dissolved in deionized water. As $\text{Bi}(\text{NO}_3)_3 \cdot 5\text{H}_2\text{O}$ undergoes decomposition in to bismuth hydroxides in water, it was first taking in 100 ml deionized water and kept on stirring. During stirring few drops of dilute nitric acid was added drop by drop until a clear and transparent solution was obtained which confirmed the complete dissolution of $\text{Bi}(\text{NO}_3)_3 \cdot 5\text{H}_2\text{O}$. Then 50 ml and 25 ml deionized water dissolved ferric nitrate and samarium nitrate were added respectively. The stoichiometric amount of tartaric acid $\text{C}_6\text{H}_6\text{O}_7$ was further added for the complete combustion of the nitrates [18, 19]. In present work tartaric acid was used as

chelating agent for the synthesis of Sm-doped BiFeO₃ nanoparticles. The uniqueness of the tartaric acid as a chelating agent in synthesis of BiFeO₃ nanoparticles probably resides in the formation of hetero-metallic polynuclear complexes in the solution, where reacting metal atoms come in close proximity. This may be arise due to the presence of two carboxylate and two hydroxyl groups with proper orientation to form a polynuclear complex, which breaks on heating in the presence of concentrated HNO₃ leading to the formation of pure phase BiFeO₃ samples. The yellow transparent solution was stirred vigorously for 12 h over a hot plate kept at 60 °C. Further the transparent solution was dried for 2 days in an oven to get the fluffy gel at temperature 95 °C. Finally, the fluffy gel was calcined at 600 °C for 2 h in furnace. The calcined powder was grinded in agate mortar and mixed with 5wt% polyvinyl alcohol as a binder to prepare the pellets using hydraulic press. The pellets were sintered at temperature 600 °C for 2 h. Samples with varying samarium (Sm) concentrations in BiFeO₃ were synthesized with the calculated empirical amount of samarium (III) nitrate hexahydrate (Sm(NO₃)₃·6H₂O) in the starting materials and followed the same process for non-doped BiFeO₃ samples. Detail about preparation processes are shown in Fig. 1.

2.3 Characterizations

The structural properties and phase identification of the prepared samples were determined using X-ray diffraction (XRD) (Shimadzu XRD-6000, Japan). The measurements were carried out at room temperature using Cu K α radiation having wavelength $\lambda = 1.5406 \text{ \AA}$, operated at 40 kV and 30 mA. The data were collected in the range $2\theta = 10^\circ$ to 110° with the step size 0.01° and the scan speed of 1° per min. Fullprof Software (Version Feb. 2012) was used for Rietveld refinement of XRD data to reveal additional structural properties of the material. Morphology of the prepared samples was examined using scanning electron microscope (JEOL Ltd., JSM-6380, Japan). The optical properties were analyzed using UV–Visible (UV–Vis) spectroscopy. The spectra were recorded over a range of 200–800 nm wavelength using Perkin Elmer Lambda-750, USA, UV–Vis-1800 spectrometer. X-ray photoelectron spectroscopy (XPS) was used by AXIS ULTRA spectrometer (Omicron

Nano Technology, ESCA⁺, Germany) with Al (ka) source to analyze the oxidation states of the samples.

3 Results and discussion

3.1 Structural analysis

3.1.1 XRD analysis

Figure 2 shows the XRD patterns of the synthesized samples confirm the phase formation and sharp and intensive diffraction peaks are observed. The sharp and intense XRD peaks signify better crystallinity of the samples. In pristine BFO sample all diffraction peaks could be similar to (JCPDS card no. 71-2494) rhombohedral phase with the space group R3c [20]. It is observed that no other secondary phase has found in the samples which indicate the reaction kinetics and thermodynamic stability of BiFeO₃ via sol–gel process. With increasing concentration of samarium XRD peaks are shifted towards higher angle 2θ which is attributed to the difference in ionic radii of Bi³⁺ (1.17 Å) and samarium (1.07 Å). The percentage of crystallinity in the samples is determined using the origin software and applying crystallinity formula.

$$\text{Crystallinity} = \frac{\text{Area of crystalline peaks}}{\text{Area of all peaks (crystalline + amorphous)}} \times 100\% \quad (1)$$

The crystalline percentage of pure and Sm-doped BiFeO₃ nanoparticle are 94.46, 97.30, 94.90, 75.69 and 66.29. It indicates that the peaks are better crystalline in nature. The enlarged view of (104) and (110) diffraction peaks are clearly separated in BFO samples as shown in Fig. 3. Nevertheless, the separate (104) and (110) diffraction peaks around 32° in pristine BFO seem to be move towards higher angles of 2θ and almost combine into a single wide peak which is clearly visible for Sm doping starting from 10% concentration, indicating that the rhombohedral BFO structure have encountered certain changes Sm substitution in agreement with previously recorded BFO doped metal ions [21–23]. These results are consistent with an increase in lattice distortion for doped nanoparticles with an increase in doping concentration, which contributes to the rhombohedral transition to the orthorhombic crystal phase. This structural distortion would be resulted from the

Fig. 1 Experimental setup diagram for the preparation of the samples

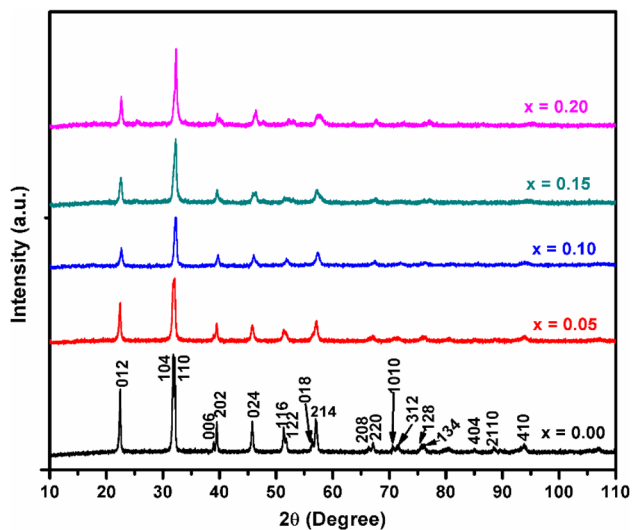
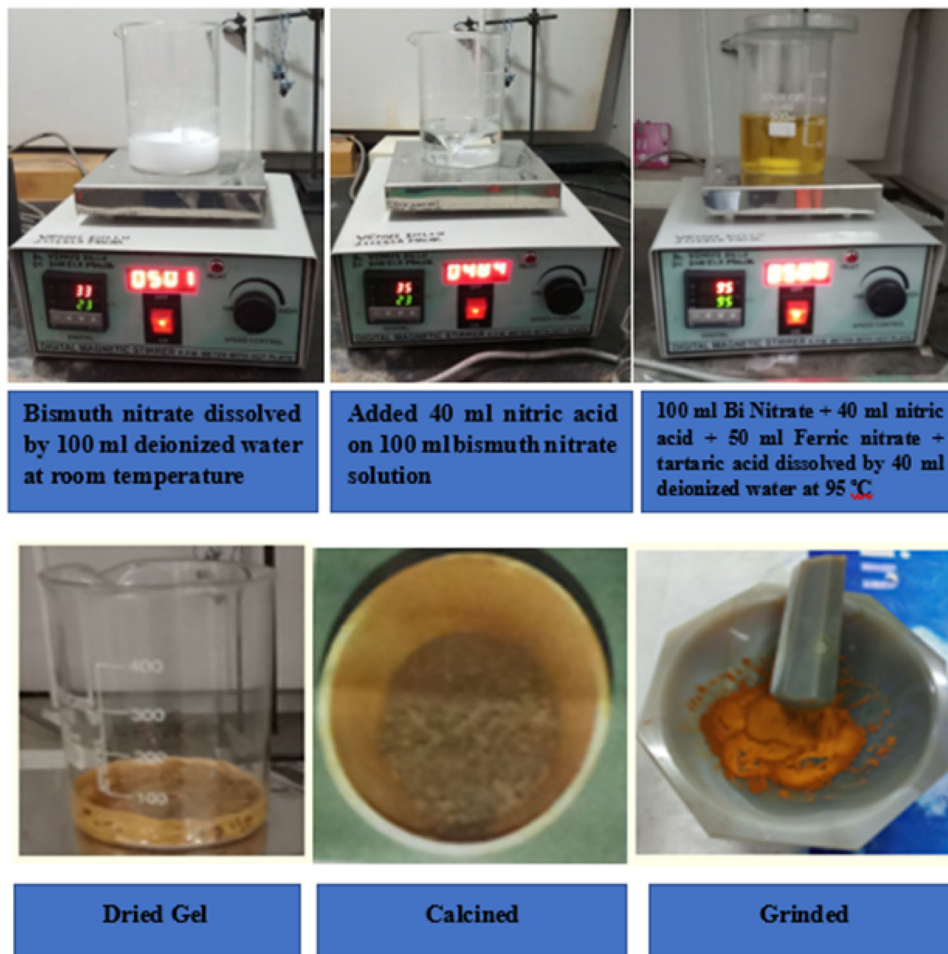


Fig. 2 X-ray diffraction (XRD) patterns of the $\text{Bi}_{1-x}\text{Sm}_x\text{FeO}_3$ samples

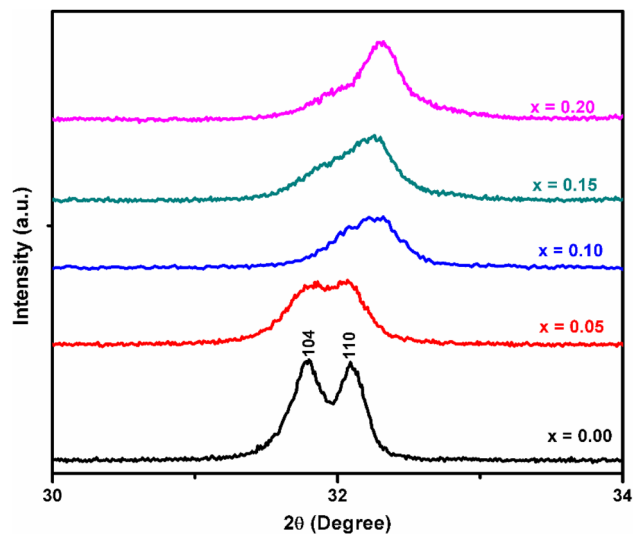


Fig. 3 Extended view of (104) and (110) XRD peak of the $\text{Bi}_{1-x}\text{Sm}_x\text{FeO}_3$ samples

differences between Bi^{3+} and Sm^{3+} ionic radii. Lattice parameters and cell volumes are presented in Table 1. It is observed that lattice parameters and cell volumes are decreased as Sm content is increasing. This indicates that there is structural transition from rhombohedral R3c space group to the orthorhombic Pnma space group phase transition. The average crystallite sizes of the samples were calculated using Debye Scherer formula [24, 25].

$$D = \frac{K\lambda}{\beta \cos \theta} \quad (2)$$

where constant K depends up on the shape of the crystallite size ($k = 0.89$), assuming the spherical shape particles, β is Full Width at Half Maximum (FWHM) of intensity (a.u.) vs. 2θ pattern, λ is the wavelength of Cu k_α radiation ($\lambda = 0.15406$ nm), θ is the Bragg's diffraction angle and D is the crystallite size. In Table 1, the size of the crystallite decreases with a raise of doping ion concentration. This indicates that the development of the lattice strain within the lattice due to an ionic size mismatches between bismuth and samarium which results in a local structural disorder and that the nucleation rate as a consequence reduces the crystallite size. Therefore, the doped BFO samples have smaller particle sizes compared to pristine BFO. The degree of distortion reduces caused by dopants was calculated using Goldschmidt tolerance factor (t) [26]

$$t = \frac{[(1-x)R_{\text{Bi}^{3+}} + xR_{\text{Sm}^{3+}}] + R_{\text{O}^{2-}}}{\sqrt{2}[R_{\text{Fe}^{3+}} + R_{\text{O}^{2-}}]} \quad (3)$$

where $R_{\text{Bi}^{3+}}$, $R_{\text{Sm}^{3+}}$, $R_{\text{Fe}^{3+}}$ and $R_{\text{O}^{2-}}$ are the ionic radius of Bi^{3+} , Sm^{3+} , Fe^{3+} and O^{2-} respectively. The tolerance factor values are listed in Table 1, implying that the distortion of the lattice increases with an increase in doping concentrations [23, 27]. The corresponding changes in the values of (t) were less than one which ensures the rotation of the FeO_6 octahedron along [111] route. It is well known that BFO crystallizes as the R3c space group rhombohedral [28, 29]. As a consequence of this doping, the lattice in the host became distorted, the rhombohedral R3c phase weakened and orthorhombic Pnma phase formed for $x = 0.05$ induced. When the concentration increased from 0.10 and 0.15 the amount of rhombohedral phase declined dramatically following a steady rise in the orthorhombic phase. An even further increase in concentration up to 0.20 contributed in the disappearance of the R3c rhombohedral phase, which was transformed in to the Pnma orthorhombic phase. This ascribed to the chemical pressure of the Sm triggered lattice distortion of the BFO host. The findings obtained are in full accordance with the existing literature on high pressure caused structural effects in BFO [30]. The Rietveld refining was conducted using the "FULLPROF" software to further examine the structural transformation.

Figure 4 demonstrates the Rietveld refinements of XRD pattern for pristine BFO. Table 1 lists the refined structural parameters along with the R-factors profile derived from the Rietveld refinement of the XRD patterns. The fitting parameters (R_f —factor, Bragg

Table 1 The average crystallite size, the average grain size, tolerance factor, lattice parameter, cell volume and the bandgap (E_g) parameter from Tauc plot for pure and doped samples

Sm doping concentration (%)	average crystallite size (D) nm	Average grain size (nm)	Tolerance factor (\AA)	Lattice parameter (\AA)	Cell volume (\AA^3)	E_g (eV)
BSFO-0	49	80	0.890	$a = b = 5.5762$ $c = 13.8615$	373.25	2.19
BSFO-5	37	60	0.889	$a = b = 5.5709$ $c = 13.8335$	371.80	2.11
BSFO-10	35	52	0.888	$a = b = 5.5559$ $c = 13.6811$	365.73	2.06
BSFO-15	33	41	0.887	$a = b = 5.5533$ $c = 13.6871$	365.54	1.98
BSFO-20	32	31	0.886	$a = 5.4885$ $b = 5.5712$ $c = 7.7698$	237.58	1.78

R-factor, and χ^2) in Table 1 indicate close coordination between the refined XRD patterns and noted. The crystalline structure of pristine BFO is standard rhombohedral structure of the space group R3c with atomic positions of Bi/Sm and Fe 6a and O 18b [31, 32]. The results of the XRD and Rietveld refinement revealed that Sm doping caused internal structure distortion related to changes in Fe–O bond distances and bond angles [33]. According to the above results, it is observed that Sm ions effectively incorporated into the crystal structure of BFO, which may play an important role in improving optical and multiferroic properties.

3.1.2 SEM analysis

Morphology of the studied $\text{Bi}_{1-x}\text{Sm}_x\text{FeO}_3$ ($x = 0.0, 0.05, 0.10, 0.15$ and 0.20) abbreviated BSFO-0, BSFO-5, BSFO-10, BSFO-15 and BSFO-20) samples are shown in Fig. 5. It is observed that the grain size of the samples varied from 30 to 80 nm. It can be seen that the average grain size of substituted samples have smaller size as compared to pristine sample as shown in Table 1. The average grain size decreases from 80 to 30 nm suggesting that the Sm content of BFO inhibits the grain growth, which can be used to control the growth of grain size. The decreased grain size may be due to bond dissociation energy of Sm–O bond (619 kJ/mole) is higher than Bi–O bond (343 kJ/mole) [34, 35]. The different radii size creates stress and strain fields that disrupt the grain growth

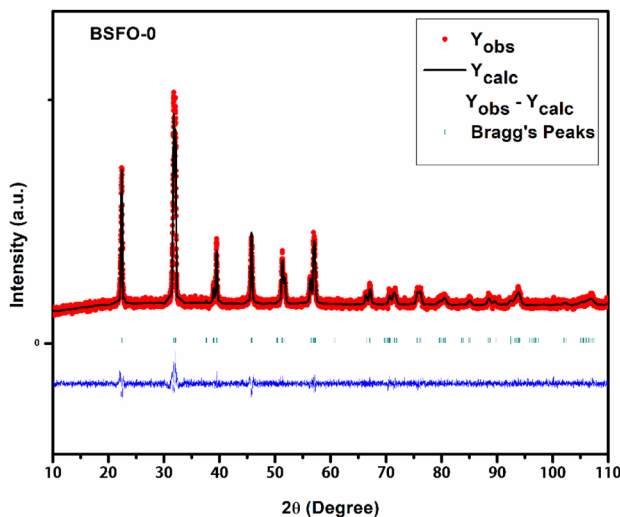


Fig. 4 Rietveld refined X-ray diffraction pattern of pristine BFO

process and cause degenerated. However, Sm doping can suppress the grain growth and expose small size of grains in the sample. This leads to increased coordination of grain and reduced porosity. In general, it is believed that the smaller the grain sizes, the more are the defects at the grain boundaries, which may have a significant influence on the optical and multiferroic properties of the nanoparticles [35, 36]. The Krikendall effect may be the another reason for decrease in grain size due to the substitution of Sm which arise due to diffusion of constituting elements of the samples [37].

3.2 Optical analysis

3.2.1 UV–Vis spectra

The optical properties of pure and Sm-doped BiFeO_3 nanoparticles were studied using UV–Vis spectroscopy. BFO is a fascinating optical material, which could be applied in photocatalyst and photoconductive devices [38]. It is well known that the optical properties are relevant to the electronic structure features and bandgap. To evaluate the optical absorption feature of photocatalysts from $\text{Bi}_{1-x}\text{Sm}_x\text{FeO}_3$ ($x = 0.00, 0.05, 0.10, 0.15$ and 0.20) samples of UV–Visible spectroscopy spectra in the wavelength range 200 to 800 nm and the examination of the samples carried out in Fig. 6. All photocatalytic samples showed substantial light absorption in both UV and Visible areas, suggesting that the $\text{Bi}_{1-x}\text{Sm}_x\text{FeO}_3$ prepared for photocatalytic reaction could react to visible light. Compared with pure BFO, an apparent blue shift can be observed in the doped samples particularly in the $x = 0.20$. As shown in Fig. 6, the photo response of the doped BFO nanoparticles has been extended in the ultraviolet and visible region, which can be used to detect ultraviolet and visible light in the photocatalysis [39]. Optical bandgaps (E_g) of pure and $\text{Bi}_{1-x}\text{Sm}_x\text{FeO}_3$ ($x = 0.00, 0.05, 0.10, 0.15$ and 0.20) samples can be calculated using the classical Tauc formula. Based on the theory of optical absorption, the relationship between both the absorption coefficient (α) and photon energy ($h\nu$) is defined as follows [40].

$$\alpha h\nu = A(h\nu - E_g)^{\frac{n}{2}} \tag{3}$$

where A is proportionality constant, E_g is the optical bandgap of the material, h is Planck’s constant, ν is the photon’s frequency, α is the absorption

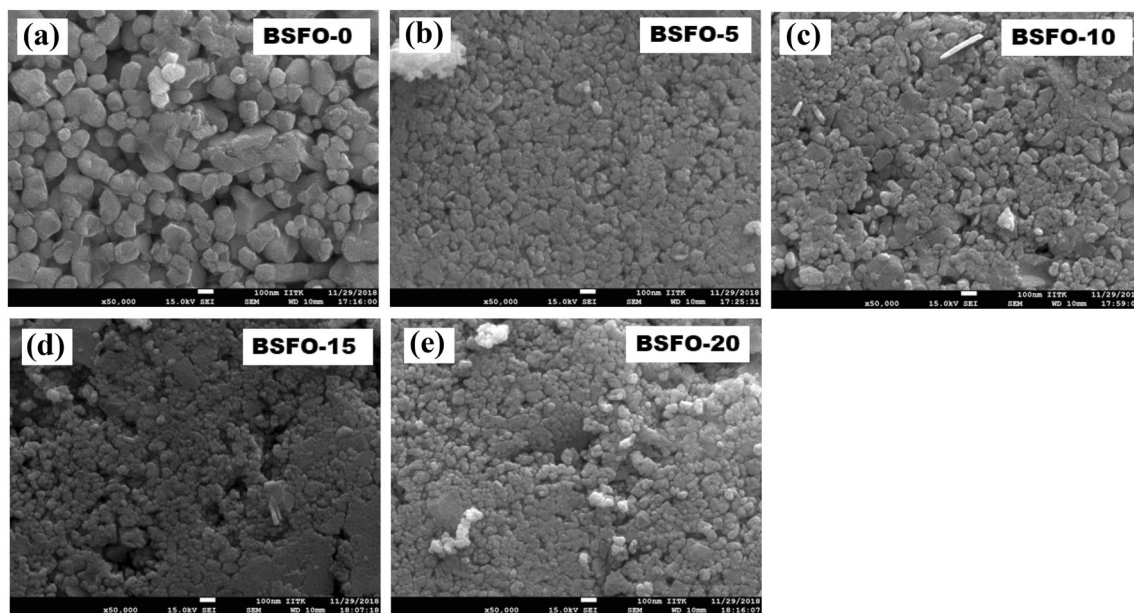


Fig. 5 Scanning electron microscope (SEM) micrograph of the $\text{Bi}_{1-x}\text{Sm}_x\text{FeO}_3$ samples

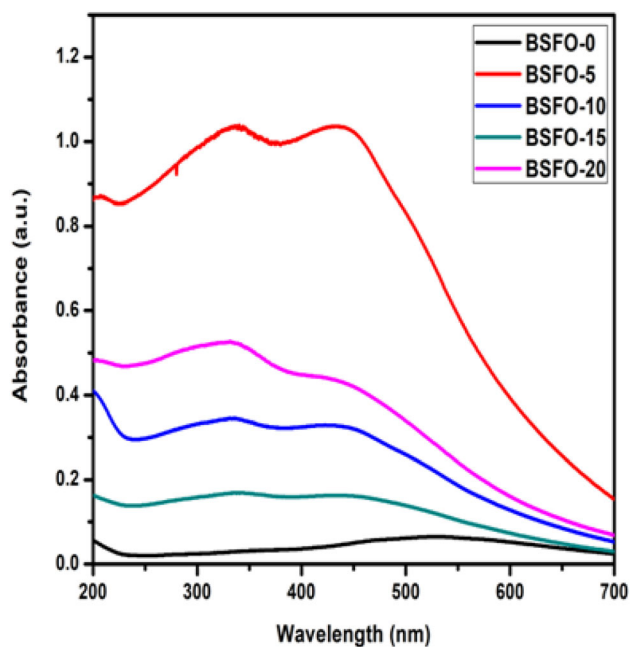


Fig. 6 UV-Vis absorption spectrum of $\text{Bi}_{1-x}\text{Sm}_x\text{FeO}_3$ nanoparticles

coefficient. The linear region of the $(\alpha h\nu)^2$ vs. $h\nu$ plots are extrapolated, $E_g = h\nu$ indirect bandgap when $(\alpha h\nu)^2 = 0$ is shown in Fig. 7. The estimated values of E_g have been depicted in Table 1. The obtained bandgap values were observed to be substantially reduced compared to thin films, which are more compatible with previous reports on pristine and

doped BFO samples [41, 42]. The decrease the bandgap may be due to molecular orbital rearrangement and distortion in octahedral FeO_6 with Samarium doping [43]. Another reason for decrease in energy badgap are the particle size and grain size has a remarkable effect on optical properties [44, 45]. In this report, the bandgap values were observed to decrease with the increase in Sm concentration, which may be caused by the change of the Fe–O–Fe bond angle and the Bi–O bond and Fe–O bond distance. The decreased energy bandgap is favorable for the photocatalytic application in the visible region [46].

3.3 XPS analysis

X-ray photoelectron spectroscopy (XPS) is an ideal method for measuring chemical composition and oxidation states of the compound components. XPS spectrum shown in Fig. 8a and b demonstrated the existence of Bi, Sm, Fe and O in the prepared samples except for a limited value of the adsorbed carbon. The C 1s peak position (284.8 eV) was used to calibrate acquired spectrum. Peaks were analyzed using XPS peak 4.1 software with the fitting function Lorentzian. The core level XPS spectrum recorded for $\text{Bi}_{0.90}\text{Sm}_{0.10}\text{FeO}_3$ and $\text{Bi}_{0.85}\text{Sm}_{0.15}\text{FeO}_3$ samples are shown in Figs. 9 and 10. Binding energies of Bi 4f7/2, Bi 4f5/2, Fe 2p3/2 and Fe 2p1/2 peaks were observed at 158.2106 eV, 163.54 eV, 158.21 eV, 163.56 eV,

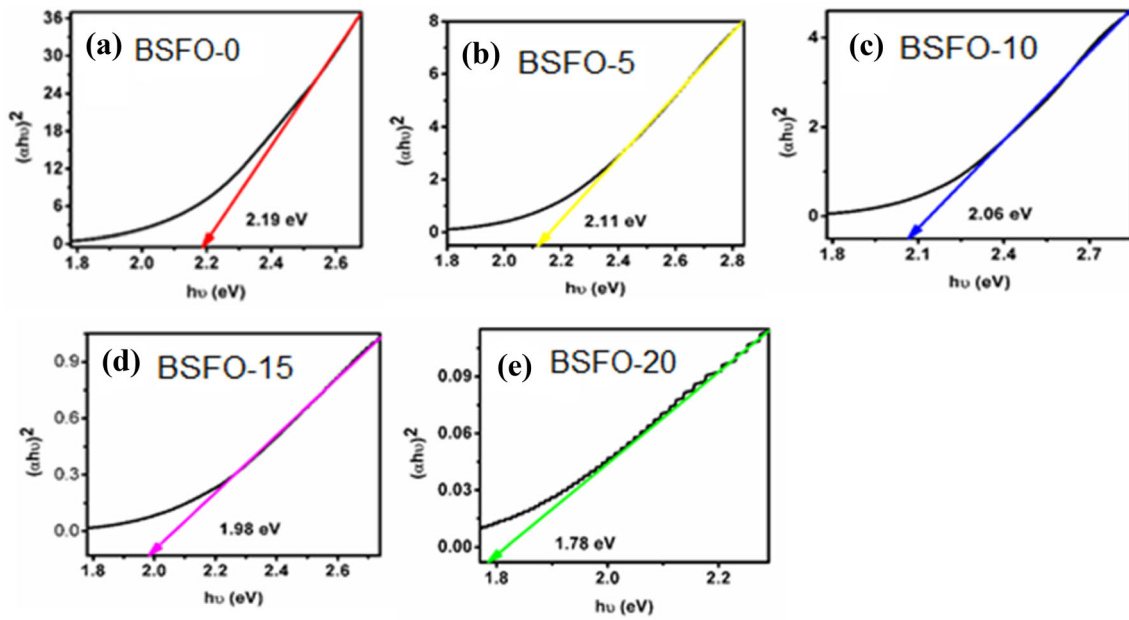


Fig. 7 Tauc plot reveal the bandgap for $\text{Bi}_{1-x}\text{Sm}_x\text{FeO}_3$ nanoparticles

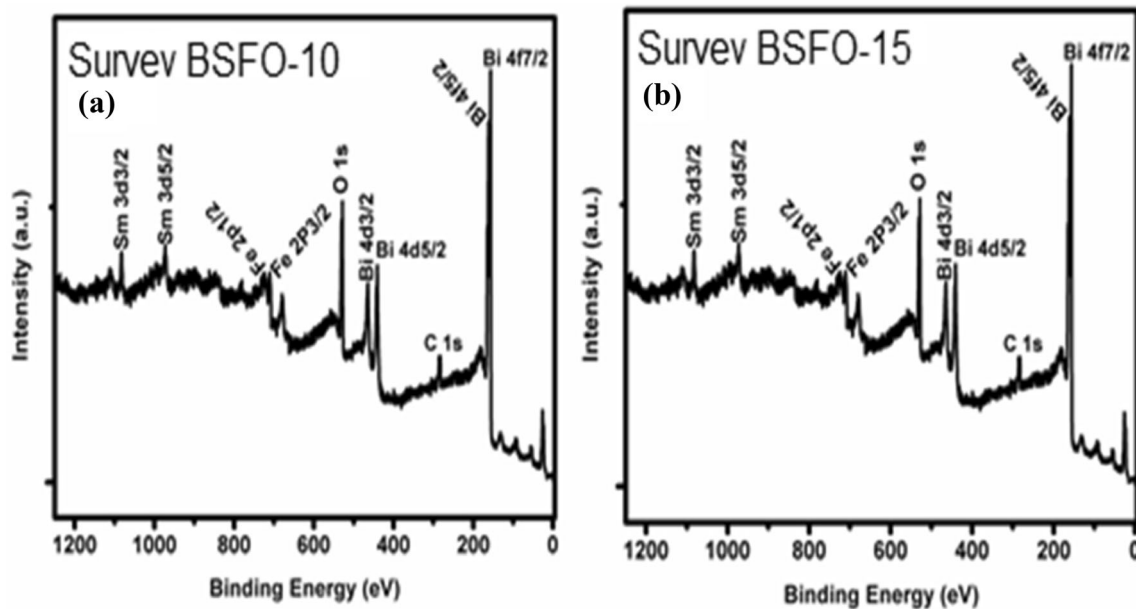


Fig. 8 XPS survey spectrum of $\text{Bi}_{1-x}\text{Sm}_x\text{FeO}_3$ nanoparticles: **a** $x = 0.10$ and **b** $x = 0.15$

711.47 eV, 723.90 eV, 711.33 eV and 723.71 eV. The Sm 3d spectra deconvoluted into two wide peaks of Sm 3d_{5/2} and Sm 3d_{3/2} at 1083.060 eV and 1110.21 eV for BSFO-10 and 1083.91 eV and 1111.26 eV for BSFO-15 shown in Figs. 9a and 10a. The advent of these observed peaks predicts dominance of the Sm³⁺ oxidation state in synthesized samples. These spectra reveal that Sm and Bi exists in its favorable + 3 state and Fe in predominant + 3 valence

state [17, 23, 28]. The two intense peaks in Bi 4f core level spectra shown in Figs. 9b and 10b at 158.20 eV, 163.54 eV (BSFO-10) and 158.21 eV, 163.56 eV (BSFO-15) are corresponding to Bi 4f_{7/2} and Bi 4f_{5/2}. The separation between the Bi 4f_{7/2} and Bi 4f_{5/2} is ~ 5.3 eV due to the spin orbit coupling indicates that Bi³⁺ oxidation state for BSFO-10 and BSFO-15 samples [47, 48]. The Bi 4f peaks in BSFO-15 sample are significantly shifted to higher binding energies

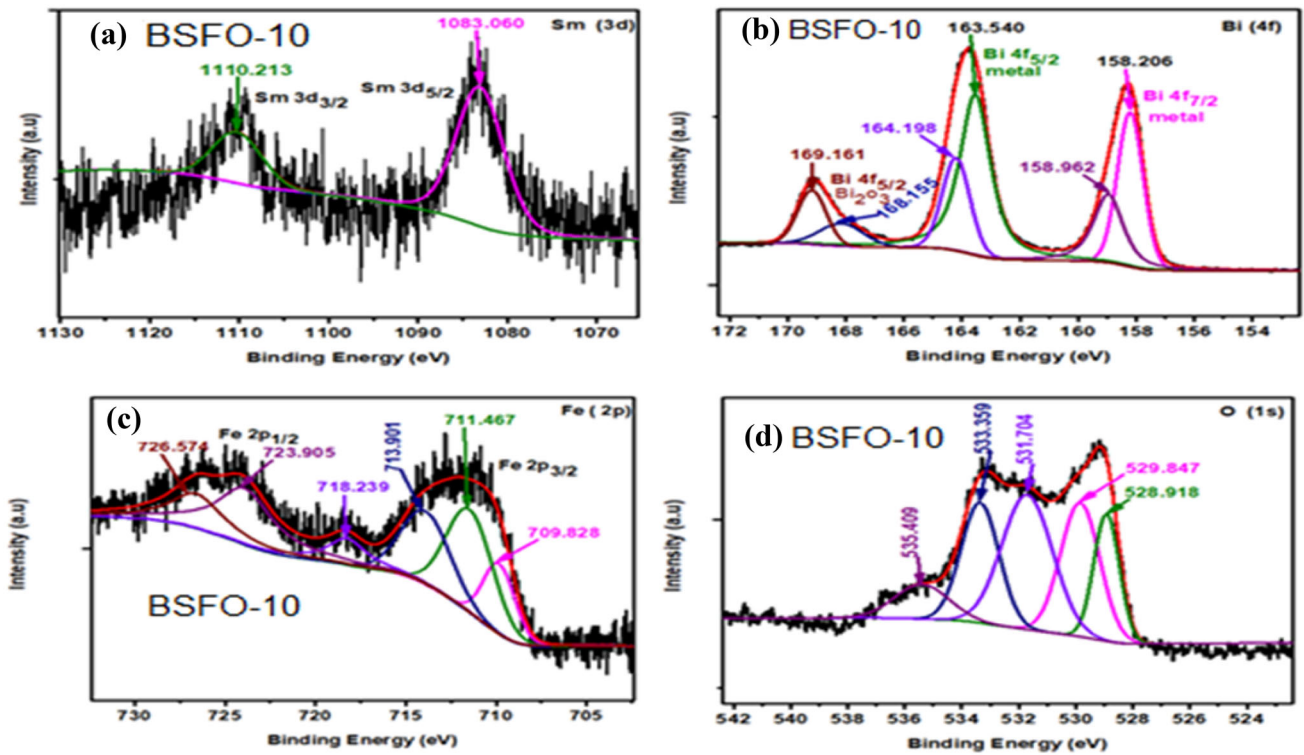
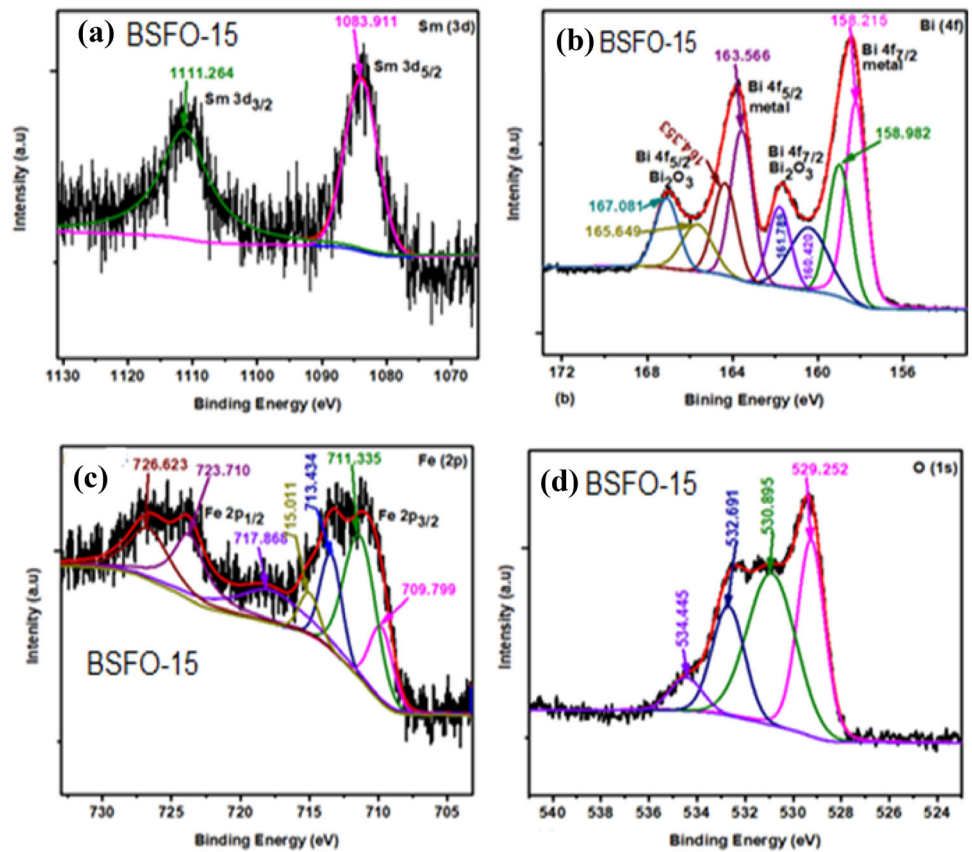


Fig. 9 Deconvoluted core level XPS spectra of **a** Sm 3d, **b** Bi 4f, **c** Fe 2p and **d** O 1s lines of $\text{Bi}_{0.90}\text{Sm}_{0.10}\text{FeO}_3$ samples

Fig. 10 Deconvoluted core level XPS spectra of **a** Sm 3d, **b** Bi 4f, **c** Fe 2p and **d** O 1s lines of $\text{Bi}_{0.85}\text{Sm}_{0.15}\text{FeO}_3$ sample



relative to the BSFO-10 sample. This shifting could be attributed to modifying Bi electronic structures [49]. The core level Fe 2p spectrum given in Fig. 9c shows that two peaks at 711.46 eV and 723.90 eV located to Fe 2p_{3/2} and Fe 2p_{1/2} and satellite peak at 718.23 eV for BSFO-10 sample. Similarly, Fig. 10c shows two peaks at 711.335 eV and 723.710 eV corresponding to Fe 2p_{3/2} and Fe 2p_{1/2} and a satellite peak at 717.86 eV approximately 8 eV above the Fe 2p_{3/2} peak for BSFO-15 sample. These results predicts the Fe³⁺ oxidation states in the Sm-doped BFO sample [50]. As we can see from Figs. 9c and 10c that Fe 2p spectrum for BSFO-10 and BSFO-15 samples were fit into multiple peaks. For BSFO-10 sample the peaks 711.46 eV, 718.23 eV, 723.90 eV and 726.57 eV and for BSFO-15 sample peaks at 711.33 eV, 713.43 eV, 715.01 eV, 717.86 eV, 723.71 eV and 726.62 eV were indicating the Fe³⁺ oxidation state, while 709.82 eV and 709.79 eV were corresponded to Fe²⁺ [51, 52]. Thus, the doping Sm³⁺ at A site in BFO restricts the hopping of Fe ions, which further leads to the suppression of oxygen vacancies and increase in the resistivity of BFO. Figures 9d and 10d shown the core level O 1s spectrum with the deconvoluted peaks centered at 528.918 eV, 529.84 eV, 531.70 eV, 533.35 eV, 535.40 eV for BSFO-10 and 529.25 eV, 530.89 eV, 532.69 eV, 534.44 eV for BSFO-15 sample correlating to the lattice oxygen (Bi–O, Fe–O bonds), oxygen vacancy, chemisorbed oxygen, and physically adsorbed oxygen [52]. The intensity of the peak around 530 eV decreases with increasing the Sm content in BFO indicating the decrease in oxygen vacancy. The above findings show the existence of Sm, Bi, and Fe in BSFO-10 and BSFO-15 samples in the states Sm³⁺, Bi³⁺ and Fe³⁺ respectively [17, 23, 28].

4 Conclusions

We have successfully synthesized Bi_{1-x}Sm_xFeO₃ samples using the sol–gel technique. The X-ray diffraction (XRD) analyses of Bi_{1-x}Sm_xFeO₃ nanocrystalline samples show the compressive lattice distortion and structural phase transformation from rhombohedral to orthorhombic phase. The particle size obtained from the XRD method were 49, 37, 35, 33 and 32 nm and the grain size obtained from SEM verifies that particles are in the range of 30–80 nm respectively. XRD and SEM measurements confirmed

the pure phase formation, nanocrystalline nature. Ultraviolet–Vis spectra of the samples show that the bandgap reduced with an increasing concentration of Sm doping. It is a suitable material for photocatalytic application. The X-ray photoelectron spectroscopy (XPS) results confirm the successful Sm doping in BFO.

Acknowledgements

The authors are grateful to MNIT JLN Marg, Jaipur and IIT Madras-Sophisticated Analytical Instrument for helping sample characterization. The authors are thankful to Ethiopian Radiation Protection Authority, ERPA and MOSHE, Ethiopia for financial support. The authors also express their gratitude to Material Research Laboratory, MRL, Sharda University, SU, India for providing chemicals and instruments for synthesizing materials for research work.

Compliance with ethical standards

Conflict of interest The authors declare that they have no conflict of interest.

References

1. G. Catalan, J.F. Scott, *Adv. Mater.* **21**, 2463 (2009)
2. V.R. Palkar, D.C. Kundaliya, S.K. Malik, *J. Appl. Phys.* **93**, 4337 (2003)
3. J.T. Han, Y.H. Huang, X.J. Wu, C.L. Wu, W. Wei, B. Peng, W. Huang, J.B. Goodenough, *Adv. Mater.* **18**, 2145 (2006)
4. J. Wang, J. Wang, J.B. Neaton, H. Zheng, V. Nagarajan, S.B. Ogale, *Science* **299**, 1719 (2003)
5. P. Ravindran, R. Vidya, A. Kjekshus, H. Fjellvåg, *Phys. Rev. B* **74**, 224412 (2006)
6. C. Ederer, N.A. Spaldin, *Phys. Rev. B Condens. Matter Mater. Phys.* **71**, 1 (2005)
7. P. Chandra Sati, M. Arora, S. Chauhan, M. Kumar, S. Chhoker, *J. Phys. Chem. Solids* **75**, 105 (2014)
8. X. Qi, J. Dho, R. Tomov, M.G. Blamire, J.L. Macmanus-driscoll, X. Qi, J. Dho, R. Tomov, *Appl. Phys. Lett.* **86**, 062903 (2005)
9. S.K. Pradhan, J. Das, P.P. Rout, V.R. Mohanta, S.K. Das, S. Samantray, D.R. Sahu, J.L. Huang, S. Verma, B.K. Roul, *J. Phys. Chem. Solids* **71**, 1557 (2010)
10. W. Mao, X. Wang, Y. Han, Y. Li, Y. Wang, Y. Ma, *J. Alloys Compd.* **584**, 520 (2014)
11. S. Godara, N. Sinha, B. Kumar, *Ceram. Int.* **42**, 1782 (2015)

12. C. Ederer, N.A. Spaldin, *Curr. Opin. Solid State Mater. Sci.* **9**, 128 (2005)
13. X. Yu, X. An, *Solid State Comm.* **149**, 711 (2009)
14. Y. Han, Y. Ma, C. Quan, N. Gao, Q. Zhang, W. Mao, J. Zhang, *Ceram. Int.* **41**, 2476 (2015)
15. H. Zhang, K. Kajiyoshi, *J. Am. Ceram. Soc.* **93**, 3842 (2010)
16. T. Zhao, A. Scholl, F. Zavaliche, K. Lee, M. Barry, A. Doran, M.P. Cruz, Y.H. Chu, C. Ederer, N.A. Spaldin, R.R. Das, D.M. Kim, S.H. Baek, C.B. Eom, R. Ramesh, *Nat. Mater.* **5**, 823 (2006)
17. R. Mazumder, P. Sujatha Devi, D. Bhattacharya, P. Choudhury, A. Sen, M. Raja, *Appl. Phys. Lett.* **91**, 1 (2007)
18. A. Azam, A. Jawad, A.S. Ahmed, M. Chaman, A.H. Naqvi, *J. Alloys Compd.* **509**, 2909 (2011)
19. J. Liu, L. Fang, F. Zheng, S. Ju, M. Shen, *Appl. Phys. Lett.* **95**, 2 (2009)
20. B.D. Cullity, S.R. Stock, *Elements of X-Ray Diffraction* (Prentice Hall, Upper Saddle River, 2001)
21. D. Dastan, *Appl. Phys. A* **123**, 1 (2017)
22. A. Jafari, M. Hosein, A. Davoud, D. Siamak, Z. Zhicheng, *J. Mater. Sci. Mater. Electron.* **30**, 21185 (2019)
23. R. Haumont, P. Bouvier, A. Pashkin, K. Rabia, S. Frank, B. Dkhil, W.A. Crichton, C.A. Kuntscher, J. Kreisel, *Phys. Rev. B Condens. Matter Mater. Phys.* **79**, 1 (2009)
24. J.I. Langford, A.J.C. Wilson, *J. Appl. Cryst.* **11**, 102 (1978)
25. V. Uvarov, I. Popov, *Mater. Charact.* **85**, 111 (2013)
26. G. Rojas-George, J. Silva, R. Castañeda, D. Lardizábal, O.A. Graeve, L. Fuentes, A. Reyes-Rojas, *Mater. Chem. Phys.* **146**, 73 (2014)
27. L. Zhang, Y. Yang, S. Ma, W. Luo, Y. Liu, K. Zhu, *Phys. B Condens. Matter* **407**, 494 (2012)
28. J.B. Li, G.H. Rao, J.K. Liang, Y.H. Liu, J. Luo, J.R. Chen, *Appl. Phys. Lett.* **90**, 1 (2007)
29. A. Mukherjee, S. Basu, P.K. Manna, S.M. Yusuf, M. Pal, *J. Mater. Chem. C* **2**, 5885 (2014)
30. P. Modak, D. Lahiri, S.M. Sharma, *J. Phys. Chem. C* **120**, 8411 (2016)
31. V. Kumar, A. Gaur, N. Sharma, J. Shah, R.K. Kotnala, *Ceram. Int.* **39**, 8113 (2013)
32. E.M.M. Ibrahim, G. Farghal, M.M. Khalaf, H.M. Abd El-lateef, *J. Nano Adv. Mater.* **5**, 33 (2017)
33. S. Gupta, M. Tomar, V. Gupta, S. Gupta, M. Tomar, V. Gupta, *J. Appl. Phys.* **115**, 014102 (2014)
34. P. Kumar, M. Kar, *Mater. Chem. Phys.* **148**, 968 (2014)
35. S. Wang, D. Chen, F. Niu, N. Zhang, L. Qin, Y. Huang, *Appl. Phys. A Mater. Sci. Process.* **122**, 1 (2016)
36. L. Leontie, M. Caraman, M. Delibas, G.I. Rusu, *Mater. Res. Bull.* **36**, 1629 (2009)
37. A. Reetu, S. Agarwal, N. Sanghi et al., *J. Appl. Phys.* **111**, 113917 (2012)
38. B. Ramachandran, M.S. Ramachandra Rao, *J. Appl. Phys.* **112**, 073516 (2012)
39. J. Zou, J. Jiang, Y. Zhang, J. Ma, Q. Wan, *Mater. Lett.* **72**, 134 (2012)
40. M. Arora, M. Kumar, *Ceram. Int.* **41**, 5705 (2015)
41. D. Dastan, P.U. Londhe, N.B. Chaure, *J. Mater. Sci. Mater. Electron.* **25**, 3473 (2014)
42. D. Dastan, N. Chaure, M. Kartha, *J. Mater. Sci. Mater. Electron.* **28**, 7784 (2017)
43. R. Shakoury, A. Arman, Ş. Tălu, D. Dastan, C. Luna, *Opt. Quant. Electron.* **52**, 270 (2020)
44. S. Farhadi, N. Rashidi, *Polyhedron* **29**, 2959 (2010)
45. K. Saravana Kumar, P. Aswini, C. Venkateswaran, *J. Magn. Magn. Mater.* **364**, 60 (2014)
46. F. Niu, D. Chen, L. Qin, N. Zhang, J. Wang, Z. Chen, Y. Huang, *ChemCatChem* **7**, 3279 (2015)
47. R. Das, T. Sarkar, K. Mandal, *J. Phys. D Appl. Phys.* **45**, 455002 (2012)
48. P.S.V. Mocherla, C. Karthik, R. Ubic, M.S. Ramachandra-Rao, C. Sudakar, *Appl. Phys. Lett.* **103**, 022910 (2013)
49. A. Mukherjee, S. Basu, L.A.W. Green, N.T.K. Thanh, M. Pal, *J. Mater. Sci.* **50**, 1891 (2015)
50. A.P. Grosvenor, B.A. Kobe, M.C. Biesinger, N.S. Mcintyre, *Surf. Interface Anal.* **36**, 1507 (2004)
51. T.D. Nguyen, D. Mrabet, T.O. Do, *J. Phys. Chem. C* **112**, 15226 (2008)
52. Y. Ding, F. Yang, L. Zhu, N. Wang, H. Tang, *Appl. Catal. B Environ.* **164**, 151 (2015)

Publisher's Note Springer Nature remains neutral with regard to jurisdictional claims in published maps and institutional affiliations.